Lab on a Chip

PAPER

View Article Online
View Journal | View Issue

Cite this: *Lab Chip*, 2025, **25**, 3803

Acoustic microstreaming and augmentation of gas exchange using an oscillating membrane towards microfluidic artificial lungs†

Anthony Mercader ‡[a] and Sung Kwon Cho *[b]

Received 30th January 2025,
Accepted 28th May 2025

DOI: 10.1039/d5lc00109a

rsc.li/loc

This paper presents a novel configuration for generating acoustic microstreaming flows at audible frequencies within a microchannel utilizing a pinned oscillating membrane. The characterization and interactions of these acoustic streaming flows with the streamwise flow within the microchannel are investigated, along with their effects on gas exchange augmentation. Advanced characterization methods and computational fluid dynamics simulations show a similar pattern and magnitude in acoustic streaming, providing evidence that this flexural membrane oscillation is the driving mechanism of the time-averaged vortices. This method exhibits potential application to microfluidic artificial lungs, particularly due to the vertical orientation of the resulting mixing, which facilitates an augmentation of gas exchange across the permeable membrane. Furthermore, it eliminates any obstructions in the microchannel and ensures stability, as opposed to other acoustic streaming methods such as sharp edge and oscillating bubble methods. Successful augmentation of gas exchange by up to 3.7× is demonstrated as shown by characterization of CO_2 transferred into the channel. Scaling up of throughput is also demonstrated with a branching design, featuring a multilayer manifold to avoid undesirable interaction of the streaming flow with the channel geometry.

Introduction

Acoustic microstreaming in concept is the generation of vortex flows from an acoustic input at small scales by interaction with certain geometric features.[1,2] The phenomenon is often used in microfluidic devices as a means to typically disrupt the strictly laminar flows seen at the micro-scale for purposes such as mixing[3] and propulsion.[4] Due to the small Reynolds numbers seen in such devices characterized by the small length scales and low velocities, viscous forces dominate, and oscillatory motion in the fluid field is usually reversible, making it difficult to generate nonzero time-averaged flows. Thus, mixing must rely on diffusion, and oscillatory motion may not result in directional net flows as it can on the macro-scale. In acoustic microstreaming, an oscillating acoustic input can interact with certain features in a flow field to generate time-averaged flows despite the small scale. It overcomes the dominance of viscous forces by introducing a higher oscillatory Reynolds number related to the oscillatory velocity at high frequency which allows inertial forces to become significant.

Many reports studying this phenomenon use ultrasound as the input[5,6] since the effect can scale positively with frequency due to higher oscillatory velocity.[7,8] The work in this article, however, focuses on audible frequency effects where the phenomenon is governed by different physics. In this regime, the acoustic wavelength is long compared to the characteristic device dimensions, and the fluid field experiences a bulk oscillation in time. There exists a more limited number of transduction methods to generate the flows from the acoustic input in this frequency range. For example, with acoustic wavelengths shorter than or on the same length scale as the fluid field, the flows are commonly driven by spatial variation of velocity within a boundary layer or spatial variation of pressure, and the pattern is related to the acoustic wavelength.[2] With a much longer acoustic wavelength, however, the fluid field experiences a bulk oscillation of pressure, and streaming is more often limited to being driven by boundary motion effects. Despite the potentially lower strength of the effect, acoustic streaming at audible frequency can carry some benefits. Lower frequency configurations can be easier and cheaper to generate with commercial actuators without requiring precise design of an interdigitated electrode, for example.[9]

[a] *Department of Mechanical Engineering and Materials Science, University of Pittsburgh, Pittsburgh, PA 15261, USA. E-mail: mercader@illinois.edu*
[b] *Department of Mechanical Engineering and Materials Science, University of Pittsburgh, Pittsburgh, PA 15261, USA. E-mail: skcho@pitt.edu*
† Electronic supplementary information (ESI) available. See DOI: https://doi.org/10.1039/d5lc00109a
‡ Current address: University of Illinois Urbana-Champaign, Urbana, IL 61801, USA.

Among these methods, the most popular is perhaps bubble streaming, where the acoustic input is tuned to a resonant frequency of a gas bubble suspended in the fluid field.[10–14] Simple volumetric or higher mode resonant oscillations cause the streaming flow due to the oscillating liquid–gas boundary. This method has advantages such as simplicity and strength. Bubbles can be trapped in the geometry of a device by pinning due to surface tension,[15] and there is flexibility in the input frequency with many available resonant modes of the bubble.[16] The disadvantages of this configuration, however, can limit application. For one, stability becomes an issue if the gas bubble dissolves into the liquid. These devices may not be able to operate indefinitely as the resonant frequency of the bubble changes with size or bubbles may dissolve entirely. Further, as many microfluidic applications are medical in nature, bubble streaming is less compatible for devices with blood as the working fluid where gas bubbles are in direct contact with blood.

More recently discovered and studied is sharp edge microstreaming.[17–19] In this configuration, either a flexible sharp edge protruding into the fluid field oscillates with some deflection, or a rigid sharp edge in the presence of strong acoustic velocity oscillation generates a pair of counter rotating vortices at the tip. The phenomenon results from a very small radius of curvature at the tip where a fluid particle driven in the direction of the tip by the oscillation is "flung" away from the tip by a centrifugal effect as it fails to track around the tip boundary. This phenomenon does not suffer from the stability issue as with bubble streaming, but the strength of the effect is typically much lower. Further, a new disadvantage is the necessity of obstruction into the fluid field which can pose issues for microchannel applications. These two streaming phenomena have even been combined to increase the overall strength,[20] though such a configuration suffers from the disadvantages of both types of streaming.

This paper presents a novel configuration to generate acoustic microstreaming flows at audible frequency using a pinned oscillating membrane and interactions of these flows with streamwise microchannel flow, which was briefly introduced in ref. 21 and 22. A schematic of this concept is presented in Fig. 1. A microchannel is formed with a thin polydimethylsiloxane (PDMS) membrane as the bottom wall, which is bonded to a rigid substrate so that a portion of the membrane is free hanging and allowed to oscillate. Acoustic energy is focused through the edge of the substrate into the free-hanging portion of the membrane, leading to flexural membrane oscillations resulting in vortex flow patterns in the fluid field above. This new configuration carries certain advantages over the previously described audible-frequency methods. It does not suffer from any stability issues like bubble streaming, nor does it require any obstruction as with sharp edge streaming. It was also found to lead to higher streaming velocity compared to the sharp edge streaming devices tested for an equivalent acoustic input. Disadvantages of the new configuration include the highly specific geometry and fabrication requirements as described. The requirement that the membrane hangs over open air limits freedom in the fabrication process, meaning that it is more suitable for an intended application where this is not detrimental, or even makes specific use of that requirement.

Comparisons can be made to some other studies, though this phenomenon maintains some distinctions from all of them. A phenomenon was briefly noted by Kolb and Nyborg among the earliest studies of acoustic streaming in the 1950s,[23,24] where a vertically vibrating tip connected to a thin film was designed such that a standing wave pattern was seen in the film. Vortex flows were observed near the tip boundary caused by a superposition of effects from both the tip velocity and film oscillation pattern, with the tip velocity being the stronger of the effects. This work does not appear

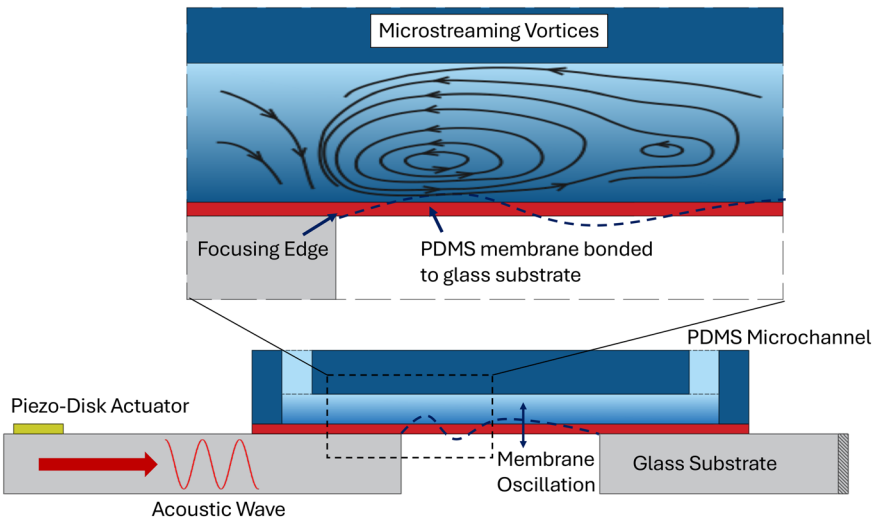

Fig. 1 Schematic diagram of the membrane microstreaming configuration.

to have any continuation since. The novel membrane microstreaming is distinct from that phenomenon in a number of ways including that the membrane oscillation is isolated as the primary driving mechanism, a more general pattern including contributions from travelling waves is allowed, and the flows are integrated into a microchannel rather than an open fluid field.

A few related modern studies are seen as well, though they tend to operate at much higher acoustic frequencies. In this case of streaming resulting from a membrane by Phan *et al.*,[25] the acoustic wavelength is on the order of the channel size. In cases of streaming resulting from surface acoustic waves, the frequency is even higher.[5,6] In such cases, the spatial pressure variation must be considered and may play a role in shaping the flow field. The use of flexural instead of acoustic waves for microstreaming has been studied using a silicon-on-nothing fabrication.[26] In this work, the driving frequency is still ultrasound with low amplitude in comparison with the proposed work and leads to pumping motion rather than vortices. Finally, the concept of an encapsulated air chamber was presented where an air is contained by a membrane and drives oscillation leading to vortex streaming.[27] The driving frequency is at around 70 kHz (ultrasound). The method of resonance is distinctive but may necessitate intricate fabrication to accommodate the volume of the air.

An intended end application for this phenomenon is microfluidic artificial lungs.[28–33] Existing commercial artificial lung devices follow the concept of the extracorporeal membrane oxygenator (ECMO), which functions by flowing blood past a bundle of permeable hollow fiber tubes containing oxygen. The microfluidic version seeks to take advantage of scaling laws by miniaturizing the blood flow and gas-permeable membrane to increase gas exchange due to the increased surface-area-to-volume ratio. These devices typically take the form of a microchannel with blood flow separated from a gas channel by a gas permeable PDMS membrane. Since these devices already feature a membrane exposed to a gas channel which would be free to oscillate, the novel membrane microstreaming concept can be naturally integrated. Active mixing through microstreaming facilitates enhanced gas transfer performance, thereby enabling the utilization of larger channel sizes. Larger channel size would greatly reduce the shear experienced by the blood, which scales harshly with the channel height, and could enable fabrication by conventional machining instead of microfabrication.

Methods

Device fabrication and operation

The fabrication process for a base configuration to generate membrane microstreaming flows is presented in Fig. 2. The standard soft lithography process is used to create molds for the microchannel profile. SU-8 2075 negative photoresist (Kayaku Advanced Materials, USA) is coated onto a Si wafer (University Wafer, USA) to a thickness in the range of 200–600 μm in one or two layers using a spin coater (WS-650MZ-23NPPB, Laurell Technologies, USA). A photomask is created featuring the microchannel profile, and the wafer is placed in a mask aligner (MA6, Karl Suss, Germany) and exposed to UV light in this shape. Finally, the wafer is placed in a bath of SU-8 developer (Kayaku Advanced Materials, USA) until only the channel profile remains in the SU-8 (Fig. 2(a)). For a 1 mm channel height, the molds are instead milled individually from an acrylic block since it would require too

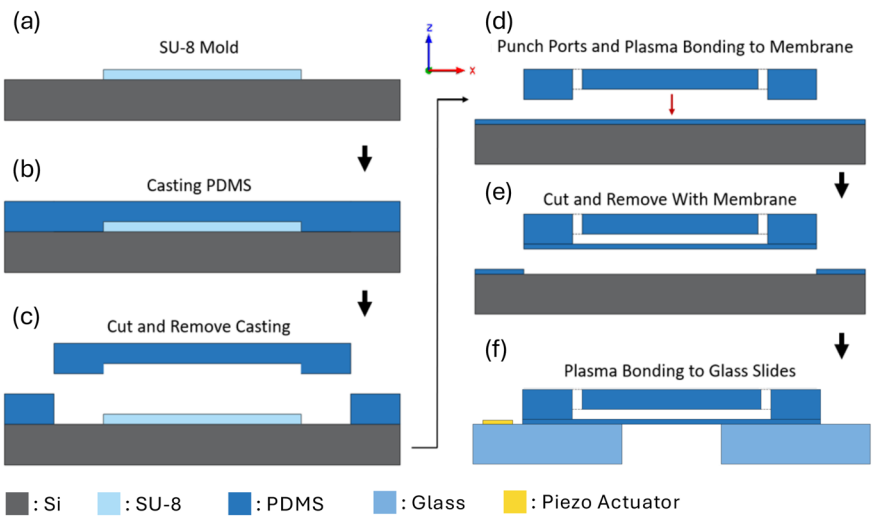

Fig. 2 Base fabrication process flow to generate membrane microstreaming flows: (a) patterning of SU-8 negative photoresist by photolithography; (b) casting of PDMS over an SU-8 mold and curing; (c) removal of the casting by cutting away with a razor blade; (d) creating inlet and outlet ports with a biopsy punch and plasma bonding to a PDMS membrane spin coated onto a Si substrate; (e) cut away bonded channel and membrane together; (f) plasma bonding of the channel to glass slides aligning over the top of the substrate edge and attachment of a piezoelectric actuator.

many layers of photoresist to create by soft lithography, sacrificing some resolution in favor of ease of fabrication. PDMS (Sylgard™ 184, Dow, USA) is then mixed in a 10 : 1 ratio of the elastomer base to curing agent, cast over the mold, and cured in an oven for 30 minutes at 90 °C (Fig. 2(b)). The channel castings are cut away from their molds using a razor blade (Fig. 2(c)), and inlet and outlet ports are created using a 1 mm biopsy punch through the thickness of the casting.

The PDMS membranes were fabricated on an Si wafer pretreated with a silanizing agent (trichloro(1*H*,1*H*,2*H*,2*H*-perflurooctyl)silane, Sigma-Aldrich, USA) by placing the wafer in a vacuum chamber with a few drops of the agent for 30 minutes and then placing the wafer on a hot plate at 150 °C for 10 minutes to evaporate away any excess, leaving a monolayer which reduces adhesion. PDMS is mixed in the same 10 : 1 ratio and spin coated onto the treated wafer to a thickness of 20 μm, and then cured in an oven for 30 minutes at 90 °C. The underside of the channel casting is bonded to the membrane by exposing both surfaces to air plasma for 1 minute each using a handheld corona plasma generator (BD-20, Electro-Technic Products, USA) and then placing the two sides together, forming a chemical bond (Fig. 2(d)). The membrane is cut around the shape of the casting with a razor blade, and the casting with the bonded membrane is peeled away from the wafer together, forming the complete microchannel (Fig. 2(e)).

The same plasma bonding process is then used to bond the underside of the membrane to a rigid glass substrate with the edge of the substrate intersecting the channel in a chosen orientation to align the streaming vortices as desired (Fig. 2(f)). In general, the axis of vortex is parallel to the edge of the substrate. The first configuration created features the glass edge aligned with the width of the microchannel (spanwise orientation (Fig. 3(a))), which is favorable for visualization and measurement. For the second configuration (Fig. 6(a)), the sidewall of the microchannel is placed directly over the top of the glass edge, aligning the streaming vortices with the length of the channel (streamwise orientation). When superimposed with streamwise channel flow, this generates helical streamlines along the length of the channel, which is less favorable for measurement, but more for the mixing application in a gas exchange device.

A piezoelectric transducer (ABZ2746B-LW100-R, PUI Audio, USA) is attached to a glass substrate with epoxy (Fig. 2(f)). The acoustic actuation is sent through the device by delivering a voltage signal to the transducer through a function generator (33500B, Keysight, USA) and amplifier (Trek PZD700, Advanced Energy, USA). To confirm the resonance frequency, the microchannel is infused with deionized water seeded with neutrally buoyant 8 μm particles (Dri-Cal DC-08, Thermo Scientific, USA) and placed in the view of a microscope and high-speed camera (Phantom v7.3, Vision Research, USA). A sine wave signal is generated by the function generator and the frequency is swept in 100 Hz increments in the range of 1–10 kHz, and then streaming velocity is observed visually by motion of the particles on a sample-by-sample basis to confirm the resonance frequency, typically in the range of 4–6 kHz.

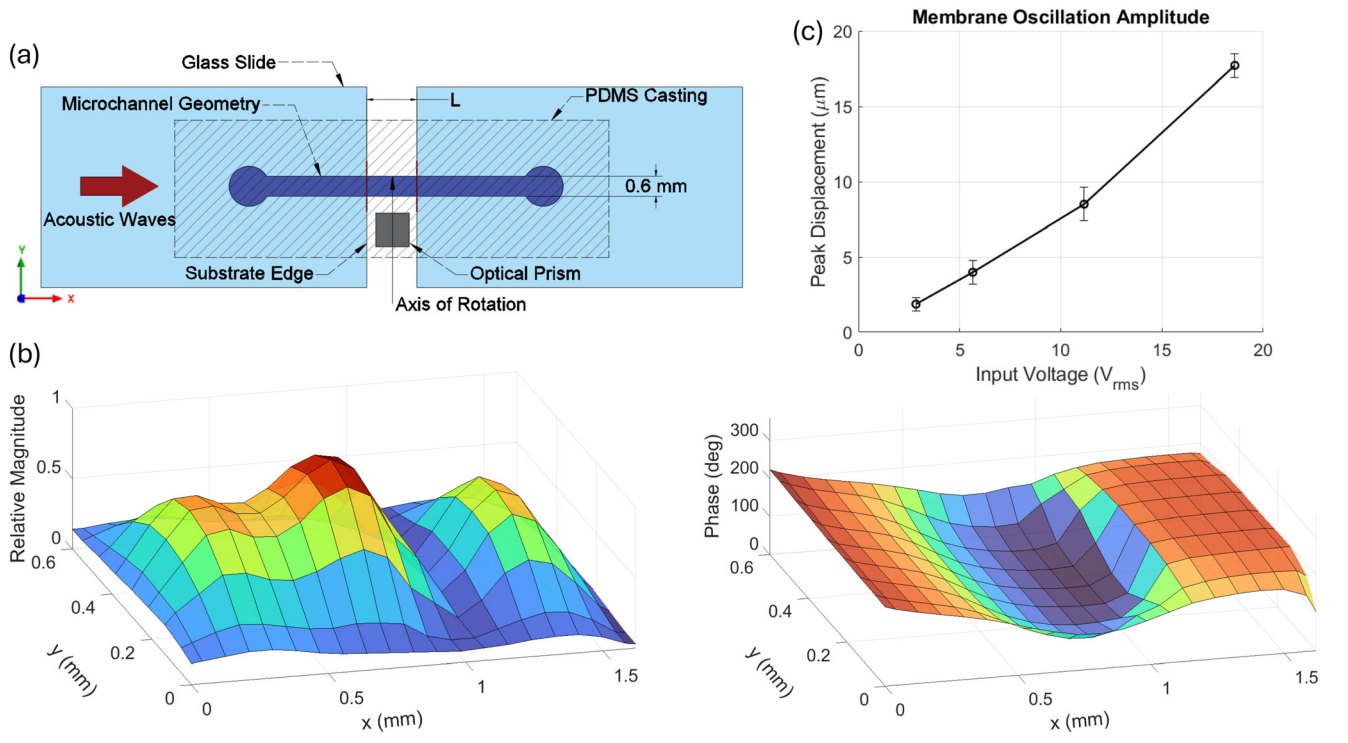

Fig. 3 (a) Top view of the testing device (the microchannel is filled with water but zero streamwise velocity, U = 0 m s^{-1}); (b) membrane oscillation magnitude and phase measured by LDV for L = 1.5, (c) membrane oscillation amplitude *vs.* input voltage.

Different time scales in flow are observed by recording at different frame rates with the high-speed camera. To observe the time-averaged microstreaming flow, footage was captured close to real time. To observe the first-order velocity oscillating at the frequency of the acoustic waves, footage was recorded well above the Nyquist frequency. For a 5.5 kHz input, footage was recorded at close to 30 000 fps, for example. With this high-speed footage, the asymmetric oscillation is visible. Particles move mainly back and forth, but the motion is not exactly reversible unlike typical with low Re flow, leading to a nonzero time averaged velocity. Example footage of particle motion at these time scales using a sample with the spanwise orientation is presented in ESI S1.†

Particle image velocimetry

Particle image velocimetry (PIV) (Dantec Dynamics, Denmark) is used to measure the velocity field of the acoustic streaming vortices. More specifically, the experiment uses micro PIV (μPIV) which routes the laser light through a microscope objective to measure flow fields at a much smaller length scale. For this technique, the fluid field is seeded with 1 μm fluorescent particles, and laser light is shined on the field at the excitation frequency of the particles in sets of two pulses at a designated time delay (D_t). Cameras are synchronized to capture images corresponding to each pulse, and then computer software then correlates the two images to calculate a velocity field in two dimensions based on the motion of the particles between the images. With the spanwise orientation samples used for characterization, the plane of interest of the velocity field requires a side view into the microchannel along the same direction of the axis of rotation of the vortices. To achieve this view, the PDMS microchannels are cast along with a right-angle optical prism (Edmund Optics, USA) to reroute the laser light and microscope view along this side view which is focused on the center plane of the channel (Fig. 3(a)).

Streaming phenomenon and characterization

Resonance characteristics and frequency selection

The strongest streaming was typically observed in the range of 4–6 kHz, confirmed by visual observation of seeded particles on a sample-by-sample basis. This range for driving frequency was chosen due to the resonance frequency of the readily available piezoelectric actuators in tandem with the resonance characteristics of the glass substrates. The nominal resonance frequency of the commonly used piezoelectric actuator was 4.6 kHz.

Modal analyses were performed using the modal analysis module in ANSYS software. Representative results from these analyses are presented in ESI S2.† A simplified geometry was created to represent either the glass substrate on its own or the substrate with the PDMS membrane and channel casting modelled by a bonded contact. It was found that the typical geometry for the glass substrate on its own had relatively low order lengthwise resonant modes, typically around 3rd order (1.5 wavelength) in that same 4–6 kHz range. It was also found that the presence of the bonded membrane and PDMS casting had a relatively minor effect on the resonance frequency and mode shape; it lowered the resonance frequency of equivalent mode shapes in the glass slide but not enough to push it out of the range of the typical frequency sweep. High amplitude deformation in the membrane corresponded to the resonant modes of the glass substrate alone, and not the resonant modes of the thin membrane which would occur at much higher frequencies. Therefore, this 4–6 kHz frequency range was chosen as a standard in all the experiments presented in this work as a match between the resonance characteristics of the actuator and substrate, but not necessarily the membrane itself.

Laser Doppler vibrometry

Characterization of the membrane oscillation (on the x–y plane in Fig. 3(a)) and fluid velocity field (on the x–z plane) is carried out in the spanwise orientation as described earlier since this orientation allowed for easier side views along the axis of rotation of the vortices. Laser Doppler vibrometry (LDV) (MSA-400, Polytec, Germany) is used to characterize the membrane oscillation. Since this method requires a reflective surface to measure, the membrane fabrication was adapted to include a 50 nm layer of titanium deposited by e-beam evaporation (MEB550S, Plassys, France) sandwiched between two 10 μm layers of PDMS, thin enough to have a minimal effect on the oscillation characteristics. The microchannel is bonded spanning two glass substrates with variable spacing. This orientation is shown in Fig. 3(a). The devices used for this test each had a resonant frequency of 5.5 kHz.

Actuation is applied at various input voltages at this frequency during measurement. The underside of the membrane is placed under the microscope objective in the LDV system, and an array of measurement points is defined across the area. The system shines laser light onto each point, and the magnitude and phase of the oscillation is measured by the reflection. An example oscillation profile for a substrate spacing of 1.5 mm, so that the entire oscillation could be captured within the 1.6 mm field of view of the LDV system, is shown in Fig. 3(b), with an animated version presented in ESI S3.† The wavelength of the oscillation (shorter than 1 mm) is much smaller than the acoustic wavelength which would be close to 20 cm in PDMS at 5.5 kHz, indicating that the acoustic input is converted into a flexural mechanical oscillation in the membrane. The peak displacement in the membrane and mechanical vibration wavelength are found to not strongly depend on the spacing between the glass substrates. This peak displacement for each input voltage measured is shown in Fig. 3(c), increasing almost linearly as the input voltage increases.

Numerical simulation and PIV measurement

A computational fluid dynamics (CFD) simulation was executed to investigate the driving mechanism of the streaming flow. The

CFX solver in ANSYS software is used, which directly solves the Navier–Stokes equations in three dimensions. A schematic of the computational domain and mesh is presented in Fig. 4(a). The fabricated channel geometry was approximated by a 600 μm × 600 μm × 10 mm rectangular prism. The prism was meshed with hexahedral elements with a nominal side length of 25 μm throughout the main volume. A mesh size inflation was specified so that the elements gradually shrink in size close to the bottom wall to a minimum thickness of 1.5 μm. Boundary conditions were applied to this geometry where the inlet and outlet were left open with no streamwise flow (U = 0 mm s^{-1}), the top and side walls were set to no-slip, and the bottom wall representing the membrane was set as a no-slip wall with specified displacement in time and space. The displacement was specified as eqn (1):

$$Y(x, y, t) = A(x, y)\cdot\cos(\omega t + \phi(x, y)), \quad (1)$$

where A is the amplitude of displacement and ϕ is the phase, both taken directly from the above LDV measurements. No information about the acoustic pressure variation is specified, nor is the substrate considered directly. The transient simulations are performed *via* the implicit second order backward Euler scheme in the CFX solver with 64 time steps per period. The streaming flow is visualized by calculating the time average of the velocity field over all the time steps in the final period. The velocity field is displayed at the center plane of the channel for direct comparison with the PIV measurements.

With the displacement magnitude and phase from the LDV data applied to CFD, the simulation results (Fig. 4(c)) show multiple vortices near the oscillating membranes, and their effect reaches almost the top wall of the microchannel.

PIV measurements are also taken in the same range of input voltage as with the LDV measurements. For each input voltage, a value for D_t is selected so that the particles in the fluid field move through an appropriate distance to be tracked by the computer software. Since the vortices are quasi-steady state, time-averaged flow resulting from asymmetric oscillations, it is important that D_t is set to an integer multiple of the acoustic period to capture each image at the same phase in the oscillation. The strongest flows characterized in these measurements required D_t to be set to 3 acoustic periods, limiting the input that could be measured by PIV, though stronger flows are possible to be generated by further increasing the input voltage.

A series of the fluorescent particle images used to calculate this velocity profile resulting from the configuration shown in Fig. 3(a) is presented in ESI S4† as a representative visualization of the vortex flow along its axis of rotation. A streamline view of the calculated flow profile is presented in Fig. 4(d). A system of two co-rotating vortices spanning the channel height is apparent with maximum velocity at the bottom of the main vortex near the oscillating membrane.

While the μPIV setup was limited to 2D planar measurements with only two components of velocity due to the single-camera setup which was routed through the microscope optics, a significant out-of-plane component of velocity is not expected to exist in this physical system. This is evidenced by the top-view visualization of the streaming flows presented in ESI S1.† This footage shows almost no component of velocity in the y-axis (channel width) relative to the in-plane vortex velocity and a relatively constant velocity field shape along that axis, except near the channel sidewalls where the no-slip boundary affects the velocity profile. The velocity field near the sidewall could unfortunately not be measured by PIV due to poor optical clarity.

Similarly, calculating the velocity field at planes of different y-axis positions within the channel in the CFD simulation results in a relatively constant pattern with the

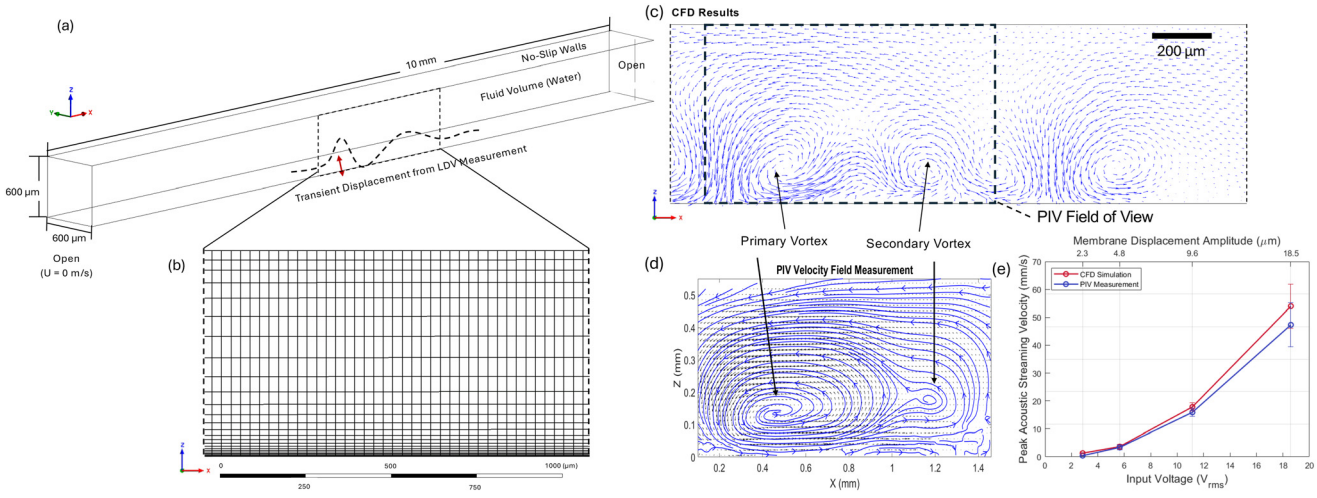

Fig. 4 (a) Schematic of CFD simulation computational domain and boundary conditions; (b) sectional view of mesh size variation along the channel height; (c) CFD simulation time-averaged velocity field; (d) velocity field measured by PIV; (e) comparison of peak velocity present in CFD simulation and PIV measurement (error bars for CFD results estimated based on variability in PIV velocity measurements).

same system of vortices only varying in velocity magnitude, again except near the channel sidewall. This indicates that the planar velocity field measurement acquired by PIV captures well the physical phenomena of interest despite the limitation of two velocity component measurement. Selecting one plane to present the velocity field from 3D simulations is representative of the trend throughout most of the region of interest except very close to the boundaries.

The results from the numerical simulation and PIV measurement are in good agreement in pattern and magnitude. The primary and secondary vortices shown in the PIV measurement are correctly predicted in the simulation. In addition, the numerical simulation predicts an additional system of counter rotating vortices farther downstream along the length of the channel, which could not be detected in the PIV measurement due to the limited field of view of the PIV system, though were present in visual observation. The input membrane displacement amplitude for the simulation is related to the input voltage in the PIV experiment through the LDV results and is plotted in the same axis by that relation for comparison in Fig. 4(e), showing good agreement in magnitude.

Both numerical simulation and PIV measurement lend evidence to the mechanical oscillation of the membrane being the driving mechanism of the streaming flows, distinguishing it from higher frequency effects which may depend on the spatial pressure gradient, for example.

Comparison to ultrasonic methods

The main physical distinction of this membrane streaming flow compared to typical ultrasonic methods is the much longer acoustic wavelength. Since the acoustic waves moving through the fluid act as a bulk oscillation, the spatial pressure gradient is negligible and does not drive a streaming flow, evidenced by the lack of the characteristic time-averaged vortices in configurations where the membrane oscillation is not present, requiring the transduction of the acoustic energy to a mechanical vibration of the membrane by the focusing edge of the substrate. There, the much shorter mechanical wavelength of the vibration allows for a spatial gradient and high enough magnitude of velocity to lead to asymmetry in the oscillation of the fluid particles, causing the time-averaged streaming flow.

Surface (SAW) or bulk acoustic waves (BAW), on the other hand, occur at the acoustic wavelength of the material at the driving frequency, which is much smaller, leading to that spatial velocity or pressure gradient on the length scale of that wavelength. A similar oscillation pattern driven by a surface or bulk acoustic wave with a wavelength matching the mechanical membrane vibration presented in this study would likely drive a streaming flow in a similar manner and could also be used to enhance gas exchange as will be explored in the following section. This is evidenced by the vast breadth of other reports studying these kinds of streaming flow in a microchannel.

While the membrane streaming configuration may not lead to some uniqueness in the shape of the vortices, there are tangible benefits to driving at much lower audible frequency in terms of cost and convenience. Audible frequency acoustic equipment is generally cheaper than ultrasound and requires much less careful design than, for example, SAW devices which necessitate a patterned interdigitated electrode with spacing selected ahead of time to match the wavelength.[9] In the audible frequency case, simply fixing the piezoelectric actuator to the substrate allows the frequency to be swept, and several resonant peaks can be visually confirmed within the search range which are related to the characteristics of the actuator.

Whether the spatial pressure gradient caused by the higher-frequency acoustic waves travelling through the fluid also contributes to the shape of the streaming vortices could be an interesting topic of investigation in future work. This could perhaps be studied better from an analytical perspective to supplement the experimental perspective provided in this work.

Gas exchange device

Orientation of vortices

Though the spanwise orientation of vortices is useful for characterization of the flow because it is easier to view along the axis (*y*-direction) of the vortices (the optical prism can be located outside of the flow channel and thus not interfere the flow), this configuration was found to have drawbacks including suboptimal mixing when combined with a streamwise channel flow in a gas exchange device. Early gas transfer tests featuring this orientation resulted in little to no performance increase when the actuation strength was increased. An effect due to closed streamlines in the vortices is proposed as a likely reason for this. In the case with no streamwise flow, the area within the vortices does indeed become well mixed. However, in the application of a gas transfer microchannel where the acoustic streaming flow is superimposed with streamwise flow, the streamlines in those vortices remain closed when the actuation is strong enough. This means that the main channel flow must be routed around these vortices. The area of closed streamlines in the vortices themselves may be well mixed, but the fluid particles within those vortices are trapped and do not contribute to the volume collected at the outlet except by limited diffusion across the streamlines on the exterior of the vortices. Further, the channel flow must "squeeze" past the vortices through a much smaller cross-sectional area, increasing the velocity and drastically reducing the residence time in the gas transfer section of the device, lowering the efficiency of gas exchange.

Another CFD simulation was adapted to visualize this effect with the spanwise vortices. For simplicity and a good streamline view, a 2D simulation was performed, presented in Fig. 5(a and b). The centerline displacement amplitude and phase from LDV measurements of a sample similar to that presented in Fig. 3(a), but with a 3 mm gap between substrate edges, were input as a boundary oscillation on the bottom wall of a 10 mm × 600 μm 2D rectangular area

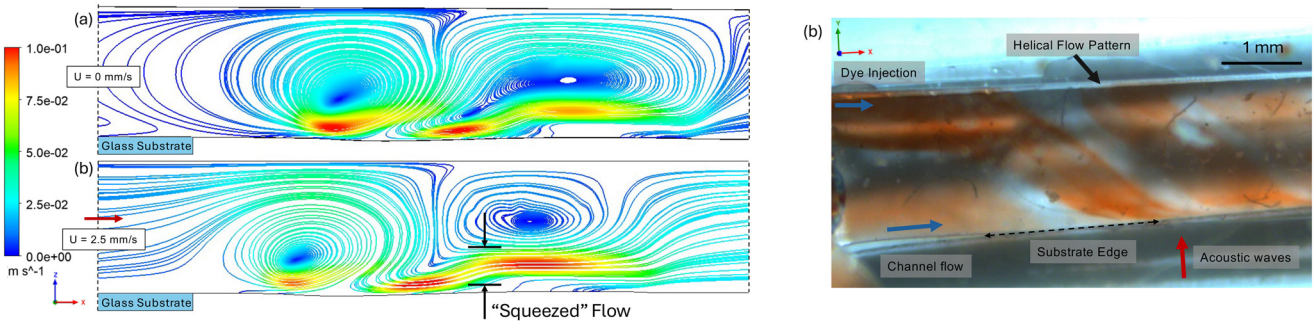

Fig. 5 (a) CFD simulation showing a squeeze effect with spanwise-oriented vortices. (b) Dye mixing visualization with a perpendicular channel orientation, resulting in helical streamlines (source video presented in ESI†).

representing the midplane of the microchannel with the same meshing parameters as the sidewall of the 3D simulation. The amplitude was scaled so the peak displacement was 16.9 μm, corresponding to the maximum value measured at an input of 18.6 V_{rms}. Streamwise flow of varying velocity, U, from left to right was included as prescribed fluid velocity on each of the left and right boundaries representing an inlet and outlet. The streamline view of these simulations is presented in Fig. 5. In the case of U = 0 mm s^{-1} (no channel flow, Fig. 5(a)), two counter rotating vortices appear which span the channel height and a maximum velocity of ~100 mm s^{-1} appears nearest the oscillating boundary. At U = 2.5 mm s^{-1} (Fig. 5(b)), representing strong streaming velocity compared to channel velocity, the squeeze effect is seen as the two main vortices maintain closed streamlines, and the main channel flow is diverted around them at a much higher velocity, undesirable in the gas exchange experiments to be described ahead.

Single channel gas exchange

For the intended end application of a gas transfer device, the fabrication process described earlier is adapted to include a channel on the underside of the permeable membrane for gas flow to infuse into the liquid side of the channel. The microchannel profile and overall device fabrication are shown in Fig. 6(a). The 1 mm thickness of the glass substrates is used as the height of the gas channel, most simply by plasma bonding the underside of the PDMS membrane to the top surface of the substrates and another PDMS layer to the underside of the substrates, respectively. As a result, the four walls of the gas channel are formed, and the PDMS membrane spans across a gap between two separate substrates. The ends of the gas channel are sealed with epoxy, and inlet and outlet ports for the gas channel are punched with a 1 mm biopsy punch on the outside of the liquid side inlet and outlet.

To avoid the squeeze effect described and promote the augmentation of gas exchange in a membrane gas transfer device, the microchannel geometry is designed to feature acoustic streaming in the streamwise orientation which results in helical streamlines when superimposed with streamwise flow as shown by a dye mixing visualization. A representative frame is presented in Fig. 5(b) with the full source video presented in ESI S5.† The single liquid channel device features a microchannel with a 15 mm length and 1.6 mm width with a constant rectangular cross section except for a small entrance and exit portion (Fig. 6(b)). Representative channel heights were selected to be 200 μm, 600 μm, and 1 mm. The resonance frequency of this device design with a 25 × 70 mm glass substrate was 5.5 kHz.

The experimental setup is shown in Fig. 6(c). A syringe pump is used to supply liquid and gas through 23 gauge PTFE tubing inserted in the inlet and outlet ports. Deionized (DI) water is supplied to the liquid side at a flow rate of 0.2 mL min^{-1} and CO_2 is supplied to the gas side at 0.4 mL min^{-1}. Liquid samples of a few drops are collected at the outlet, and the pH is measured with a micro pH electrode to estimate CO_2 transfer through the permeable PDMS membrane and into the liquid channel *via* a similar correlation to that presented in ref. 34. The input voltage to the piezoelectric actuator is varied from 0–45.5 V_{rms} during the flow.

The gas transfer results are presented in Fig. 6(d). For each channel height tested, there is a significant increase in CO_2 concentration in the liquid samples as the actuation strength is increased, showing that active mixing by acoustic streaming enhances the gas transfer through the permeable membrane into the channel as expected. Further, the relationship of the channel height is changed when actuation is present compared to the results with no actuation (0 V_{rms}). With no actuation, the gas transfer performance decreases as the channel height increases. This is according to expectation due to the fact that a taller channel will tend to be more diffusion limited due to the lower surface area to volume ratio, although there is a competing effect of lower velocity at a given flow rate, and therefore a larger residence time of the liquid over the membrane. However, even at the smallest input voltage tested, the 600 μm channel height shows the highest output concentration of CO_2 when the actuation is present, up to 3.7× compared to that at 0 V_{rms}. The shortest channel tested, at 200 μm, shows the smallest relative improvement. Finally, the tallest 1 mm channel tested shows a large relative improvement in output concentration. However, this improvement does not overcome the gap in performance present with no actuation.

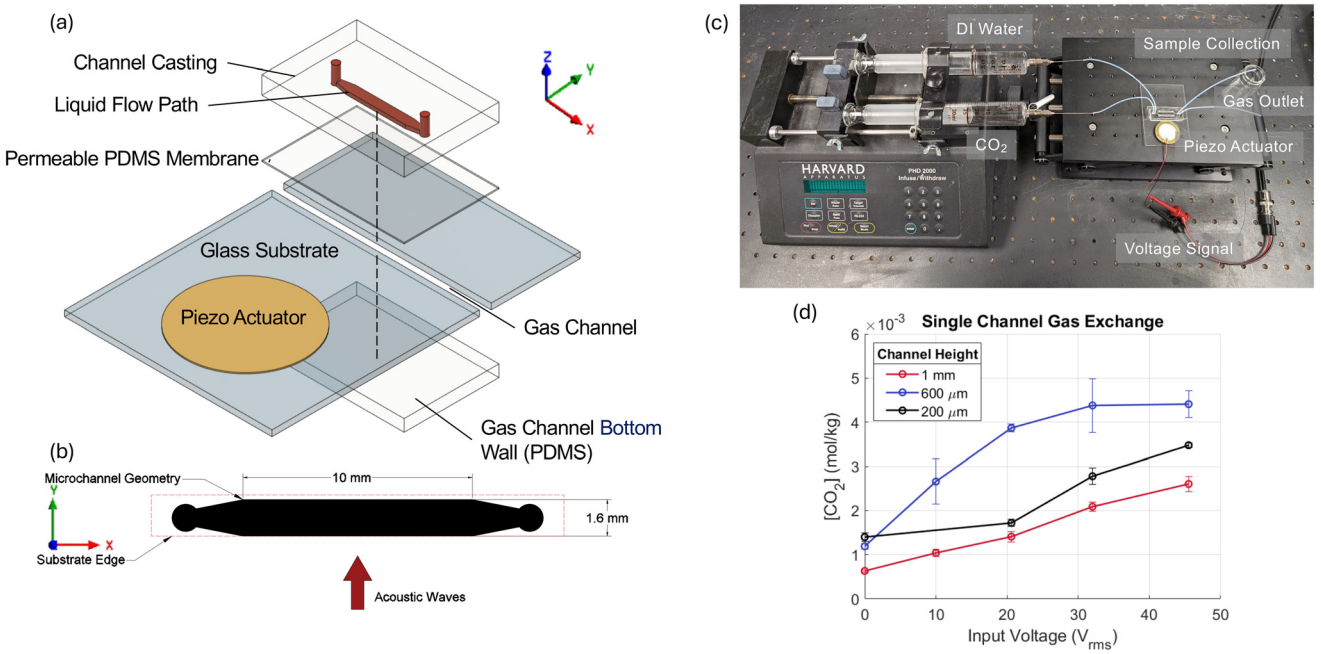

Fig. 6 (a) Single channel gas exchange device fabrication; (b) microchannel profile; (c) picture of the experimental setup; (d) gas exchange results.

In terms of the total gas exchange rate into the channel, the best case of the 600 μm height channel saw an improvement from 252 mL_{CO_2} min^{-1} m^{-2} in the passive case to 936 mL_{CO_2} min^{-1} m^{-2} for the highest level of actuation tested. These values enable a brief comparison to other artificial lung studies. As presented in ref. 28, representative first generation artificial lung devices featured a gas exchange rate in the range of 12–329 ml_{O_2} min^{-1} m^{-2} into blood. Therefore, the device presented in this work features a similar gas exchange rate to these studies in the passive case, but improves the performance significantly beyond that level in the active case. Of course, those studies represent a more challenging configuration of gas exchange into veinous blood which already features an appreciable concentration of O_2, whereas the DI water used as the input in this work was mostly devoid of dissolved gas. The comparison is nonetheless encouraging for future iterations of this device which will test gas exchange into blood, and a more detailed performance comparison will be appropriate at that time.

These results indicate that there exists an optimal channel height to balance the competing factors, which likely contains the entire height of the vortices so that the entire volume of the channel experiences good mixing. This is in line with the original goal for the experiment, demonstrating the dual benefit of this method: the gas transfer performance is increased outright with actuation present and favors a larger than minimum channel height despite the reduced surface area to volume ratio.

Mechanism of augmentation of gas exchange

The augmentation of gas exchange is majorly attributed to the mixing flow generated by acoustic streaming. More specifically, in the passive case corresponding to no actuation of the membrane, the gas exchange is limited by diffusion due to the strictly laminar nature of microfluidic channel flow with parallel streamlines. In that case, gas transferred into the liquid side of the channel through the membrane faces a strong barrier to diffusion into the fluid volume in the *z*-axis, and a continuous gradient of gas concentration exists in the liquid channel with the highest concentration near the gas transfer membrane and the lowest concentration near the top channel wall.[29,35] This leads to a relatively smaller gas concentration gradient across the membrane itself, reducing the exchange through that membrane. For the selected geometric parameters used in these experiments, the contribution of the membrane to the resistance to mass exchange is negligible compared to the contribution of diffusion in the liquid channel for the passive case.[36]

The potential contribution of the membrane deformation during the actuation to the augmentation of gas exchange was examined and determined to be negligible. Briefly, nonporous PDMS does exhibit a change in permeability dependent on biaxial stretch related to a change in the microstructure through which the mass transfer occurs, but this only becomes significant in a regime of hyperelastic deformation.[37] The strain experienced in these experiments is well within the low-deformation, linear elastic regime due to the thin, flexible nature of the membrane with small amplitude oscillation compared to its length, and the permeability can be assumed constant. This combined with the already negligible contribution of the membrane to the resistance to mass exchange indicates that targeting diffusion within the liquid channel is the only viable strategy to augment gas exchange for these selected geometric parameters.

With the introduction of mixing in the liquid side channel by the acoustic streaming flows in a favorable orientation, the concentration of gas within the liquid is spread, bringing liquid volumes with lower concentration of gas into closer proximity to the gas exchange membrane due to the nature of the helical streamlines, resulting in a higher average concentration gradient across the membrane itself. This leads to a higher average magnitude of gas exchange.

Branching channel

For the intended end application of microfluidic artificial lungs, it is important that the gas transfer device is able to expand to support an indefinite number of branching channels since a single channel device cannot support the total throughput required while maintaining similar gas transfer efficiency. To this end, later tests are focused on scaling up the gas exchange device with a branching channel geometry. An improved device design was necessary to allow for multiple glass edges on a single substrate to serve as sites to generate acoustic streaming sites and result in a more compact overall design. To this end, custom substrates were created by modification of commercial glass slides to include multiple through holes to serve as the gas channel volume and as passthrough holes to transport gas to the underside gas channel. A schematic of this gas exchange device with branches is presented in Fig. 7(a). With support from the University of Pittsburgh Glass Shop (RRID: SCR 023719), this pattern of through holes was realized on commercial 75 × 50 × 1 mm^3 glass slides by CO_2 laser ablation in many passes on the low wattage setting. A simple PDMS channel casting was again created by soft lithography to route the gas from the passthrough holes to the gas channel cutouts and plasma bonded on the underside of the substrate. A microchannel mold was created, which features two branches with a similar gas transfer area compared to the previous single channel tests. The profile is shown in Fig. 7(b).

The fabricated device showed strong acoustic streaming at a resonant frequency of 4 kHz. The experimental parameters were the same as with the single channel experiments, but with double the liquid and gas flow rates in hopes that the performance would be comparable at double the throughput. The gas transfer results are shown in Fig. 7(c) with the previous 600 μm height results for comparison. A slight increase in gas transfer was observed for low input voltage, but a drastic reduction in performance was observed at high actuation strength, performing much worse than even the unactuated baseline for this fabrication. The reduction in performance was repeated after the experiment was fully reset.

It is theorized that this reduction in performance is related to the previously discussed squeeze effect. Though the main gas transfer section features glass edge sites in the streamwise orientation, the branching geometry of the channel necessitates a transition where the underside of the membrane crosses that edge (Fig. 7(b)), meaning the lengthwise orientation is not perfectly maintained around these transition zones. In this case, the angling of the streamwise channel flow relative to the substrate edge redirects the acoustic streaming vortices to have a significant component of velocity aligned with the streamwise direction. When the actuation strength is increased, a significant enough fraction of the liquid channel volume features vortices with closed streamlines to reduce the gas transfer

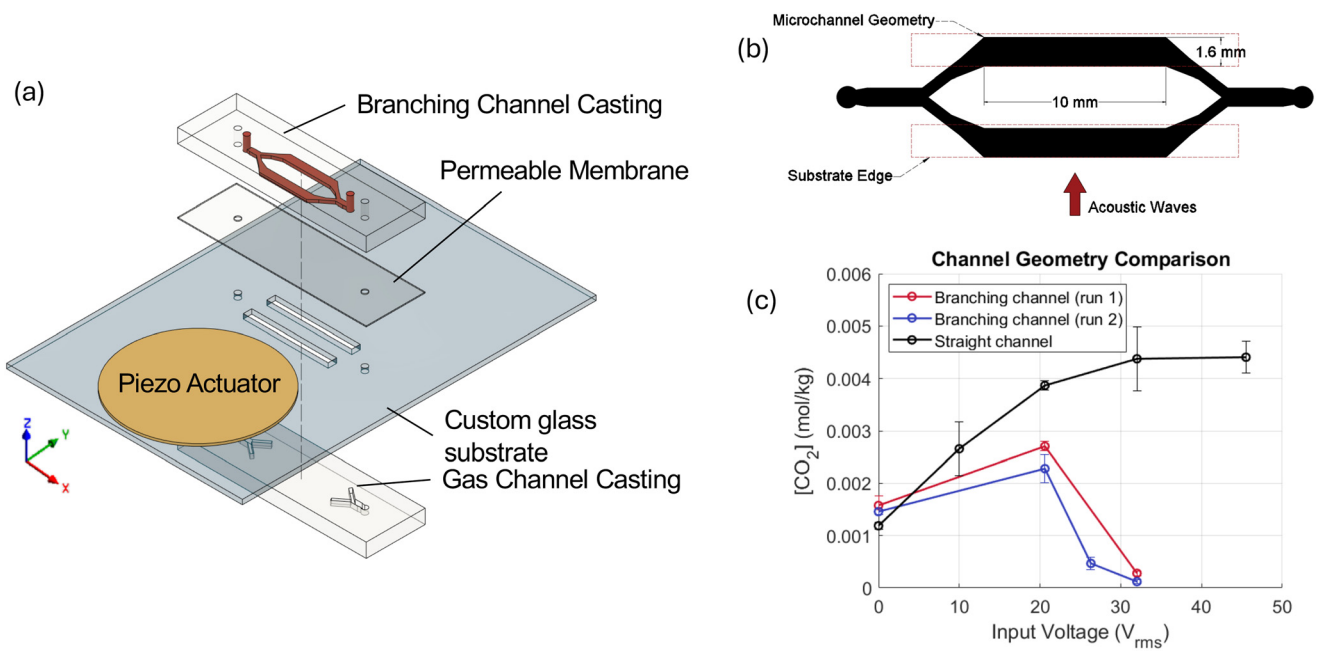

Fig. 7 (a) Schematic of the gas exchange device with branches; (b) initial branching channel geometry; (c) gas transfer results showing reduced performance.

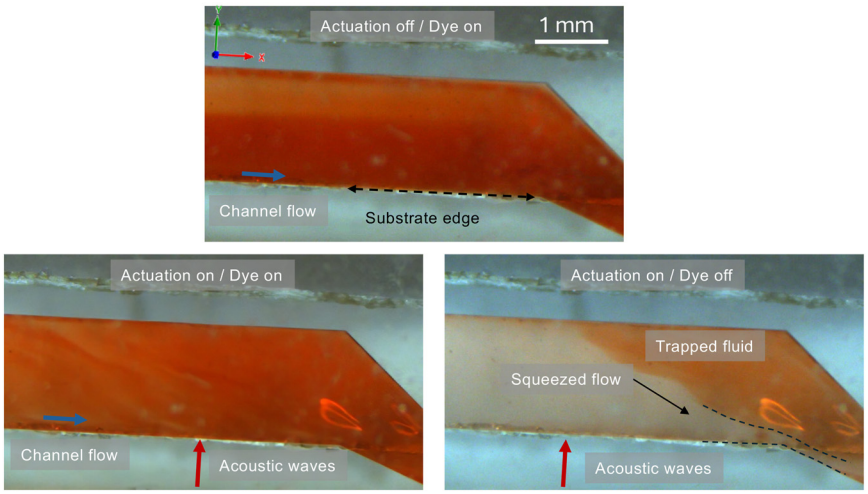

Fig. 8 Dye mixing visualization of interaction between acoustic streaming flow and streamwise channel flow with angled channel geometry showing a large pocket of fluid trapped in closed vortices and main channel flow diverted around when dye injection is stopped (source video presented in the ESI†).

performance by forcing the main channel flow around these trapped fluid particles at higher velocity.

The effect is visualized by a dye mixing experiment. Representative frames are shown in Fig. 8 with the full source video presented in ESI S6.† A thin needle is used to punch holes through the PDMS casting to inject dye in the channel while streamwise flow of DI water is input *via* a syringe pump through the inlet. Footage is recorded at the exit portion of the gas transfer area. With no actuation, the fluid is poorly mixed downstream due to reliance exclusively on diffusion. When actuation is turned on, the fluid appears well mixed as helical streamlines form in the main gas transfer section. Near the exit of the gas transfer section, however, a vortex is also formed with an axis of rotation in the direction perpendicular to the angled channel wall, and therefore perpendicular to the streamwise flow. When dye injection is stopped, a clear delineation forms between the well mixed area in this vortex where the dye is trapped in closed streamlines and a portion of the streamwise flow is squeezed around the vortex through a very thin cross-sectional area. It is theorized that if the acoustic streaming vortices are strong enough compared to the streamwise velocity, a significant enough portion of the gas transfer area is compromised with suboptimal mixing, leading to the overall reduction in gas transfer efficiency observed in the branching channel gas transfer tests. For a gas exchange device, it is desirable that the acoustic streaming vortices avoid any component of velocity parallel to the streamwise flow.

Manifold design

With the effect of the vortex orientation in mind, it was necessary to redesign the multichannel geometry to avoid this angling problem in relation to the transition from the substrate to gas transfer area. However, it was difficult or maybe impossible to design a channel geometry in a single layer which both avoided this angled transition and allowed for an indefinite amount of edge sites for the membrane microstreaming flow.

A manifold fabrication concept was designed to fulfil these requirements. A schematic of the fabrication concept is presented in Fig. 9(a). This design includes one additional layer of PDMS casting to serve as a manifold to supply multiple individual liquid channels on the gas transfer layer, each with a straight channel geometry identical to the prior single channel device shown in Fig. 6(a). The main channel layer casting includes two individual single channels with defined spacing to match the holes in the custom substrate. Holes punched in these castings serve as an interface with the manifold layer on top. The manifold layer was created again by soft lithography and features a channel design that routes liquid from a unified inlet and outlet and branches to supply each individual channel's inlet and outlet at the punched interface. The substrate and gas side channel are identical to the previous iteration. Since the channel branching occurs on a layer separated from the glass substrate and supplies each individual gas transfer channel from above directly over the top of the breathing holes, the angled transition of channel flow from the substrate area to the gas transfer membrane area is avoided, and the substrate edge to focus the acoustic energy can be kept perfectly straight in the lengthwise orientation. The resulting acoustic streaming flow is then similar to the previous single channel gas transfer tests.

The gas transfer test was again performed with the same parameters as in the single channel experiments, but with double the liquid and gas flow rates. The results are presented in Fig. 9(b). Now, the relationship to both input voltage and channel heights is similar to that in the single channel experiments. Each channel height tested shows an improvement in gas exchange as the actuation strength is increased, and the taller channels are favored compared to the

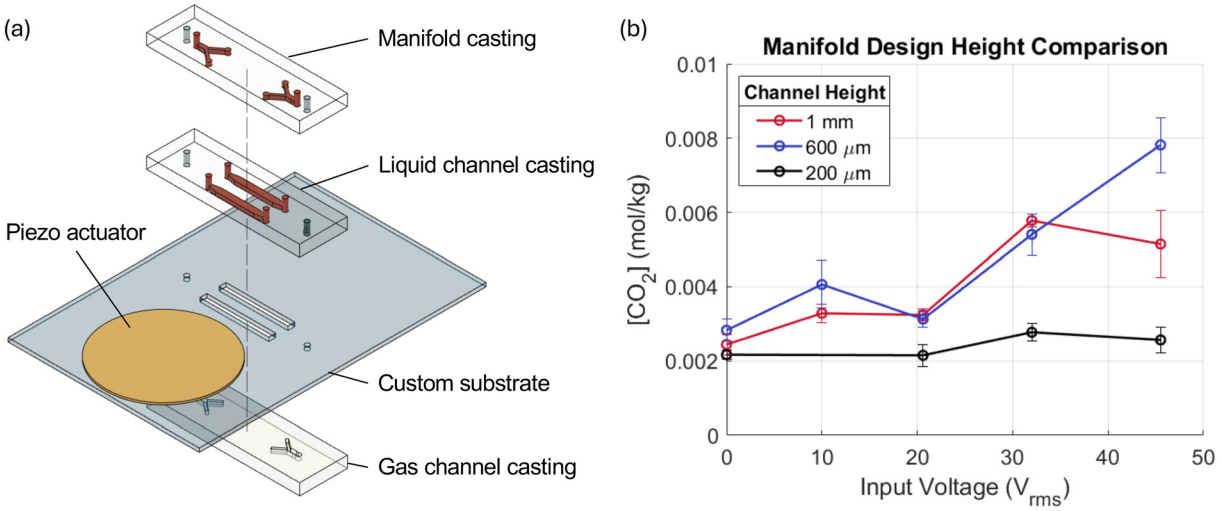

Fig. 9 (a) Schematic of the manifold dual channel gas transfer device; (b) manifold dual channel gas transfer results.

200 μm channel despite their lower surface-area-to-volume ratio. Specifically, the 600 μm channel performs best, with an increase in estimated CO_2 concentration of 2.8×, compared to the case with no actuation. This once again indicates that the optimal height exists which contains the entire diameter of the vortices. This time, the data appear to be more noisy, likely due to more inconsistent fabrication of the more complex design, but the trends hold.

The fabrication here features only two branches as a proof of concept due to the fabrication by hand of each sample, but an important feature is that the manifold can be adapted to support an indefinite number of branches where each supplies a single channel over a breathing hole in the substrate with exactly the same geometry. It would be possible with dedicated manufacturing to scale the number of channels up to meet a total throughput requirement that might be impossible with a single channel.

Conclusions

This work presents an investigation on a novel configuration to generate acoustic streaming flows in a microchannel using an oscillating membrane and the interaction of this acoustic streaming with the channel geometry and streamwise flow in relation to the performance of a gas transfer device. The streaming flows are generated when an acoustic input is focused through the edge of a substrate into a mechanical oscillation of a thin membrane, resulting in time-averaged vortex flows in the fluid field of a microchannel above. This kind of microstreaming flow has advantages over other kinds of streaming in the lower frequency range where the acoustic wavelength is large compared to the device geometry, including stability compared to bubble streaming and lack of obstruction compared to sharp-edge streaming. The concept is suited to certain end applications including a membrane gas transfer device such as the microfluidic artificial lung concept, where a membrane placed above a gas channel is already a design requirement.

The driving mechanism of the acoustic streaming flow is investigated by characterization of the membrane oscillation and flow field and comparison to CFD simulation. LDV is used to measure the amplitude and phase of oscillation across the membrane area. PIV is used to measure the 2D velocity field or representative samples. The shape of the vortices is detailed as a system of vortices with the peak velocity nearest the membrane and the streaming strength is related to the voltage input to the piezo actuator. The membrane oscillation pattern is input as a boundary motion in a CFD simulation where the time-averaged velocity field results are comparable in pattern and strength to the PIV measurements. This indicates that the membrane oscillation caused by focusing of the acoustic energy into the membrane from the substrate edge is the primary driving mechanism of the streaming flow, rather than any effect from the spatial pressure gradient as is seen with higher-frequency acoustic streaming phenomena.

The streaming concept is integrated into a proof-of-concept gas transfer device where the permeable membrane is used to generate the streaming, separate liquid and gas microchannels, and transfer gas into the liquid side. This device features the membrane bonded to the glass substrate in an orientation so that the vortex flows have an axis of rotation parallel to the channel length, leading to helical streamlines when superimposed with the streamwise flow. Gas transfer in the actuated channel is improved up to 3.7× compared to the non-actuated case.

Suboptimal performance in an angled, branching channel led to a more detailed investigation on the interaction between the channel geometry, acoustic streaming patterns, and streamwise flow. It was found that the angled channel geometry and the transition where the microchannel crosses the substrate edge can lead to streaming flows with a significant component of velocity parallel to the streamwise

flow. This can lead to a squeeze effect where fluid particles are trapped in the closed streamlines of the vortices, and the main channel flow is diverted around at a much faster velocity. When the streaming velocity is strong enough in this case, a significant enough portion of the gas transfer area is compromised, leading to an overall reduction in gas transfer performance.

Finally, a manifold fabrication concept is designed to support indefinite branching channels and membrane streaming sites while avoiding this squeeze effect. Gas transfer tests with a two-channel design show comparable performance at double the flow rates compared to the single channel test, an important step towards scaling up the device to support the throughput required by microfluidic artificial lungs. Similar to the single-channel tests, the taller microchannels are favored when actuation is added. This can be leveraged to support higher throughput with less shear experienced by the liquid, potentially beneficial if blood is to be used as the working fluid. The taller channels are also possible to be fabricated by conventional machining methods rather than the more complex and expensive photolithography, as demonstrated by the fabrication of 1 mm channels by CNC milling.

This first work on the topic is intended to detail the physical phenomena of the streaming and resulting mixing with an example application to gas exchange towards microfluidic artificial lungs to look forward to. Hence, only gas transfer into deionized water here was investigated with a focus on those physical phenomena, avoiding any complications that would result from the variable nature of biological samples. Future work on this project is directed towards furthering the application of microfluidic artificial lungs. Tests will be adapted to feature blood as the working fluid, specifically investigating the compatibility of blood with the streaming flow in terms of coagulation, platelet deposition, and oxygenation performance. Future work will demonstrate the capability to oxygenate blood to biological levels despite using taller channel heights than other microfluidic artificial lung studies. Furthermore, it will provide quantitative comparison of the gas channel efficiency to those in other studies.

Data availability

The data that support the findings of this study are available from the corresponding author (Sung Kwon Cho) upon reasonable request.

Author contributions

SKC initiated/supervised the project and reviewed/revised the manuscript. AM performed the experiments and simulations, analyzed the data, and drafted/revised the manuscript.

Conflicts of interest

There are no conflicts of interest to declare.

Acknowledgements

This work is in part supported by the NSF (ECCS-2325000) grant.

References

1 S. Sadhal, Acoustofluidics 13: Analysis of acoustic streaming by perturbation methods, *Lab Chip*, 2012, **12**(13), 2292–2300.
2 M. Wiklund, R. Green and M. Ohlin, Acoustofluidics 14: Applications of acoustic streaming in microfluidic devices, *Lab Chip*, 2012, **12**(14), 2438–2451.
3 C.-Y. Lee, *et al.*, Microfluidic mixing: a review, *Int. J. Mol. Sci.*, 2011, **12**(5), 3263–3287.
4 J. Feng and S. K. Cho, Mini and micro propulsion for medical swimmers, *Micromachines*, 2014, **5**(1), 97–113.
5 M. K. Tan, L. Yeo and J. Friend, Rapid fluid flow and mixing induced in microchannels using surface acoustic waves, *EPL*, 2009, **87**(4), 47003.
6 G. Destgeer, *et al.*, Adjustable, rapidly switching microfluidic gradient generation using focused travelling surface acoustic waves, *Appl. Phys. Lett.*, 2014, **104**(2), 023506.
7 J. Friend and L. Y. Yeo, Microscale acoustofluidics: Microfluidics driven via acoustics and ultrasonics, *Rev. Mod. Phys.*, 2011, **83**(2), 647.
8 M. B. Dentry, L. Y. Yeo and J. R. Friend, Frequency effects on the scale and behavior of acoustic streaming, *Phys. Rev. E*, 2014, **89**(1), 013203.
9 T.-D. Luong, V.-N. Phan and N.-T. Nguyen, High-throughput micromixers based on acoustic streaming induced by surface acoustic wave, *Microfluid. Nanofluid.*, 2011, **10**, 619–625.
10 P. Tho, R. Manasseh and A. Ooi, Cavitation microstreaming patterns in single and multiple bubble systems, *J. Fluid Mech.*, 2007, **576**, 191–233.
11 D. Ahmed, *et al.*, A millisecond micromixer via single-bubble-based acoustic streaming, *Lab Chip*, 2009, **9**(18), 2738–2741.
12 C. Wang, S. V. Jalikop and S. Hilgenfeldt, Efficient manipulation of microparticles in bubble streaming flows, *Biomicrofluidics*, 2012, **6**(1), 012801.
13 J. Feng, J. Yuan and S. K. Cho, Micropropulsion by an acoustic bubble for navigating microfluidic spaces, *Lab Chip*, 2015, **15**(6), 1554–1562.
14 F.-W. Liu and S. K. Cho, 3-D swimming microdrone powered by acoustic bubbles, *Lab Chip*, 2021, **21**(2), 355–364.
15 A. Marin, *et al.*, Three-dimensional phenomena in microbubble acoustic streaming, *Phys. Rev. Appl.*, 2015, **3**(4), 041001.
16 D. Gritsenko, *et al.*, Vibrational modes prediction for water-air bubbles trapped in circular microcavities, *Phys. Fluids*, 2018, **30**(8), 082001.
17 P.-H. Huang, *et al.*, An acoustofluidic micromixer based on oscillating sidewall sharp-edges, *Lab Chip*, 2013, **13**(19), 3847–3852.
18 N. Nama, *et al.*, Investigation of acoustic streaming patterns around oscillating sharp edges, *Lab Chip*, 2014, **14**(15), 2824–2836.
19 A. A. Doinikov, *et al.*, Acoustic streaming produced by sharp-edge structures in microfluidic devices, *Microfluid. Nanofluid.*, 2020, **24**(5), 32.

20 M. R. Rasouli and M. Tabrizian, An ultra-rapid acoustic micromixer for synthesis of organic nanoparticles, *Lab Chip*, 2019, **19**(19), 3316–3325.
21 A. L. Mercader and S. K. Cho, Stable, Obstruction-Free, Audible Frequency Acoustic Streaming by a Pinned Oscillating Membrane, in *Acoustofluidics 2022*, 2022, Glasgow, Scotland, UK, pp. 132–133.
22 A. L. Mercader and S. Kwon Cho, Strong Microstreaming from a Pinned Oscillating Membrane and Application to Gas Exchange, *2023 IEEE 36th International Conference on Micro Electro Mechanical Systems (MEMS)*, Munich, Germany, 2023, pp. 1025–1028.
23 J. Kolb and W. L. Nyborg, Small-scale acoustic streaming in liquids, *J. Acoust. Soc. Am.*, 1956, **28**(6), 1237–1242.
24 W. L. Nyborg, Acoustic streaming near a boundary, *J. Acoust. Soc. Am.*, 1958, **30**(4), 329–339.
25 H. V. Phan, T. Alan and A. Neild, Droplet manipulation using acoustic streaming induced by a vibrating membrane, *Anal. Chem.*, 2016, **88**(11), 5696–5703.
26 P. Vachon, S. Merugu, J. Sharma, A. Lal, E. J. Ng and C. Lee, Investigation of Localized Flexural Lamb Wave for Acoustofluidic Actuation and Particle Control, *2021 IEEE International Ultrasonics Symposium (IUS)*, Xi'an, China, 2021, pp. 1–4.
27 N. F. Laubli, *et al.*, Embedded microbubbles for acoustic manipulation of single cells and microfluidic applications, *Anal. Chem.*, 2021, **93**(28), 9760–9770.
28 J. A. Potkay, The promise of microfluidic artificial lungs, *Lab Chip*, 2014, **14**(21), 4122–4138.
29 T. Kniazeva, *et al.*, Performance and scaling effects in a multilayer microfluidic extracorporeal lung oxygenation device, *Lab Chip*, 2012, **12**(9), 1686–1695.
30 W.-I. Wu, *et al.*, Lung assist device: development of microfluidic oxygenators for preterm infants with respiratory failure, *Lab Chip*, 2013, **13**(13), 2641–2650.
31 K. Kovach, *et al.*, In vitro evaluation and in vivo demonstration of a biomimetic, hemocompatible, microfluidic artificial lung, *Lab Chip*, 2015, **15**(5), 1366–1375.
32 A. J. Thompson, *et al.*, Design analysis and optimization of a single-layer PDMS microfluidic artificial lung, *IEEE Trans. Biomed. Eng.*, 2018, **66**(4), 1082–1093.
33 T. L. Astor and J. T. Borenstein, The microfluidic artificial lung: Mimicking nature's blood path design to solve the biocompatibility paradox, *Artif. Organs*, 2022, **46**(7), 1227–1239.
34 K. Wood, The pH-CO2 relationship in natural waters: With 2 figures and 1 table in the text, *Verh. - Int. Ver. Theor. Angew. Limnol.*, 1978, **20**(1), 54–58.
35 Z. Wu, N.-T. Nguyen and X. Huang, Nonlinear diffusive mixing in microchannels: theory and experiments, *J. Micromech. Microeng.*, 2004, **14**(4), 604.
36 J. A. Potkay, A simple, closed-form, mathematical model for gas exchange in microchannel artificial lungs, *Biomed. Microdevices*, 2013, **15**, 397–406.
37 A. R. Spitzer and S. B. Hutchens, Deformation-dependent polydimethylsiloxane permeability measured using osmotic microactuators, *Soft Matter*, 2023, **19**(31), 6005–6017.